The Astrophysical Journal, 720:46–63, 2010 September 1 doi:10.1088/0004-637X/720/1/46

SPITZER OBSERVATIONS OF IC 2118

S. Guieu[1,10], L. M. Rebull[1], J. R. Stauffer[1], F. J. Vrba[2], A. Noriega-Crespo[1], T. Spuck[3], T. Roelofsen Moody[4,11], B. Sepulveda[5], C. Weehler[6], A. Maranto[7], D. M. Cole[1], N. Flagey[1], R. Laher[1], B. Penprase[8], S. Ramirez[9], and S. Stolovy[1]

[1] Spitzer Science Center/Caltech, M/S 220-6, 1200 E. California Blvd., Pasadena, CA 91125, USA
[2] U.S. Naval Observatory, Flagstaff Station, 10391 West Naval Observatory Rd., Flagstaff, AZ 86001-8521, USA
[3] Oil City Area Senior High School, 10 Lynch Blvd., Oil City, PA 16301, USA
[4] Bassick High School, 1181 Fairfield Avenue, Bridgeport, CT 06605, USA
[5] Lincoln High School, Stockton, CA 95207, USA
[6] Luther Burbank High School, San Antonio, TX 78204, USA
[7] McDonogh School, Owings Mills, MD 21117, USA
[8] Pomona College, 333 North College Way, Claremont, CA 91711, USA
[9] NASA Exoplanet Science Institute, IPAC, M/S 1002-22, 1200 E. California Blvd., Pasadena, CA 91125, USA
Received 2009 December 4; accepted 2010 June 30; published 2010 August 5

ABSTRACT

IC 2118, also known as the Witch Head Nebula, is a wispy, roughly cometary, ∼5 degree long reflection nebula, and is thought to be a site of triggered star formation. In order to search for new young stellar objects (YSOs), we have observed this region in seven mid- and far-infrared bands using the *Spitzer Space Telescope* and in four bands in the optical using the U. S. Naval Observatory 40 inch telescope. We find infrared excesses in four of the six previously known T Tauri stars in our combined infrared maps, and we find six entirely new candidate YSOs, one of which may be an edge-on disk. Most of the YSOs seen in the infrared are Class II objects, and they are all in the "head" of the nebula, within the most massive molecular cloud of the region.

Key words: circumstellar matter – infrared: stars – ISM: clouds – ISM: individual objects (IC 2118) – stars: formation – stars: pre-main sequence

Online-only material: color figures

1. INTRODUCTION

Our general understanding of how and why stars form rests upon the answers to a set of basic questions: given a particular locale, how, why, and when did stars form there? Current theory tells us that in some regions, stars simply collapse under the influence of their own natal clouds' gravity, but in others, the process may be heavily influenced by external events such as nearby supernovae, which may prompt parts of the cloud to form stars. Many people have searched for evidence of triggered star formation on large and small scales (e.g., Briceño et al. 2007, and references therein). In the cases where triggered star formation is suspected, a complete inventory of the young stars formed by the cloud is useful specifically to (1) search for evidence of sequential star formation within the cloud and with respect to other nearby clouds, and (2) within the individual cloud, understand the initial mass function (IMF), the total mass in the cloud versus stars, and the star formation efficiency. The former strengthens (or weakens) the case for having found legitimate triggered star formation, and the latter allows closer study of the initial conditions of star formation (e.g., Ballesteros-Paredes et al. 2007). If the specific cloud does turn out to be forming stars as a result of triggering, then a detailed comparison of the IMF and star formation efficiency for a triggered cloud versus a cloud that has collapsed under its own gravitational influence will shed further light on the mechanics of star formation itself.

Finding all of the young stars in any given cloud in the optical can be problematic due to extinction from the cloud itself. However, the *Spitzer Space Telescope* (Werner et al. 2004) provides an excellent platform for surveying star-forming regions in the mid-IR and far-IR, enabling stars with IR excesses to be identified in a relatively straightforward fashion, even those embedded fairly deeply in the cloud. Because *Spitzer* efficiently maps large regions of the sky, it is a particularly useful tool for surveying clouds subtending relatively large areas.

IC 2118 (Kun et al. 2001, 2004), the Witch Head Nebula, is ∼5 degrees long; its "wind-blown" appearance is similar in the optical and infrared—see Figure 1 for the wide-field optical image from the Palomar Observatory Sky Survey. It has been cited as an example of triggered star formation. The specific distance to the object is somewhat controversial. If it is close to ∼400 pc, the trigger could be the Trapezium (Lee & Chen 2007). If, instead, it is closer, some ∼200 pc away, the possible trigger is the Orion–Eridanus superbubble (Kun et al. 2001, 2004), and the cloud is likely to be additionally excited by β Orionis (Rigel, at 264 pc; van Leeuwen 2007). It is possible that interactions with both the expanding superbubble and the winds from Rigel (both to the East of IC 2118) create the cometary shape of the nebula. For the rest of this paper, we take the distance to IC 2118 to be 210 pc (Kun et al. 2001), although we comment more on this distance uncertainty below.

Some authors previously have noted star formation in this region; Kun et al. (2001) summarizes all previously identified objects here, including red nebulous objects found by Cohen (1980). With a ^{12}CO survey of the IC 2118 region, Kun et al. (2001) detected six molecular clouds which include MBM 21 and MBM 22 (G 208.4-28.3 and G 208.1-27.5, respectively). Kun and collaborators (Kun et al. 2001; Kun & Nikolic 2003; Kun et al. 2004) conducted an objective prism survey with spectroscopic follow-up to search for new T Tauri stars in the

[10] Current address: European Southern Observatory, Alonso de Córdova 3107, Casilla 19001, Vitacura, Santiago 19, Chile; sguieu@eso.org.
[11] Currently at New Jersey Astronomy Center, Raritan Valley Community College, Somerville, NJ, USA

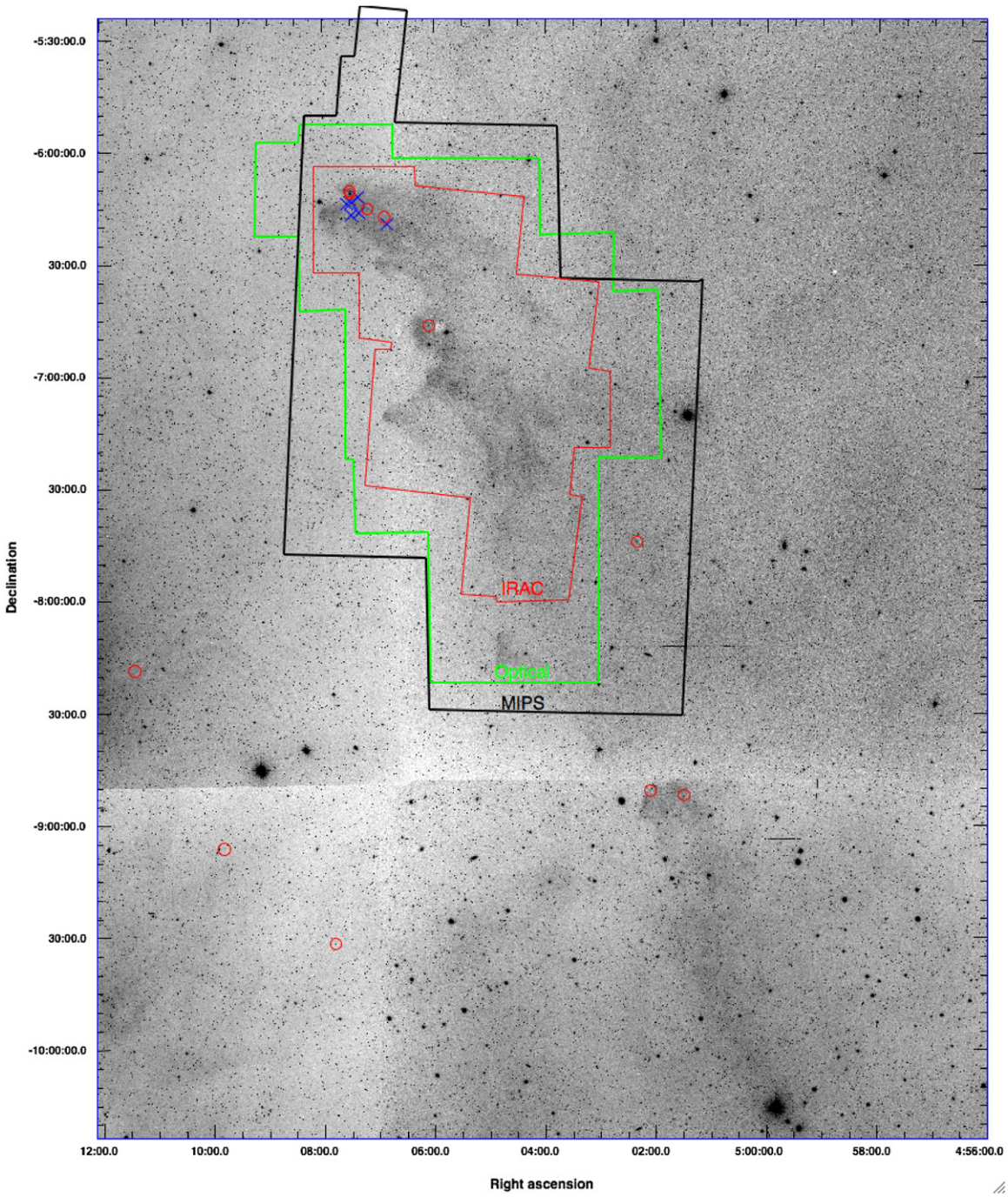

Figure 1. Palomar Observatory Sky Survey (POSS) red image of IC 2118, with the 11 previously identified T Tauri stars indicated (red circles), as well as the six new candidate YSOs found here (blue ×). The outlines of our IRAC (red), MIPS (black), and optical (green) observations are included for reference.

IC 2118 region. They concluded that there are 11 young stars in the vicinity, 8 of which they discovered, and 6 of which are located within (projected onto) the higher-density nebulosity of the cloud; see Table 1 (where all the types come from Kun et al. (2004)) and Figure 1. Based on this census of YSOs in IC 2118, the star formation efficiency here was taken to be ∼3%.

We used *Spitzer* to survey the heart of the IC 2118 region, with the Infrared Array Camera (IRAC; Fazio et al. 2004) at 3.6, 4.5, 5.8, and 8 microns, and the Multiband Imaging Photometer for *Spitzer* (MIPS; Rieke et al. 2004) at 24, 70, and 160 microns. In this paper, we use these data to search for candidate young stellar objects (YSOs) with infrared excesses. We use our additional optical and Two-Micron All-Sky Survey (2MASS; Skrutskie et al. 2006) photometric data in an effort to segregate YSOs from background galaxies. While one previously known T Tauri star appears without an excess in our MIPS map alone, we find infrared excesses in four of the five previously known T Tauri stars in our combined IRAC and MIPS maps, and we find six entirely new candidate YSOs.

The observations and data reduction are described in Section 2. We select YSO candidates using *Spitzer* colors in Section 3, and discuss their overall properties in Section 4. Finally, we discuss some wider implications and summarize our main points in Section 5.

Table 1
Previously identified T Tauri Stars in IC 2118

Name	R.A. (J2000)	Decl. (J2000)	Spectral Type[a]	Other names
IRAS 04591−0856	05 01 30.2	−08 52 14	...	HHL 17, G13
2MASS 05020630−0850467	05 02 06.3	−08 50 47	M2 IV	...
RXJ 0502.4−0744[b]	05 02 20.8	−07 44 10	...	2MASS 05022084−0744099
2MASS 05060574−0646151[c]	05 06 05.7	−06 46 15	G8:	(May not be a member of IC 2118; see Kun et al. 2004)
2MASS 05065349−0617123[c,d]	05 06 53.5	−06 17 12	K7 IV	...
2MASS 05071157−0615098[c,d]	05 07 11.6	−06 15 10	M2 IV	IRAS F05047−0618
2MASS 05073016−0610158[c,d]	05 07 30.2	−06 10 16	K6 IV[e]	IRAS 05050−0614, Kiso Hα A0974−19, RNO 37
2MASS 05073060−0610597[c,d]	05 07 30.6	−06 11 00	K7 IV[e]	Kiso Hα A0974−20, RNO 37
RXJ 0507.8−0931	05 07 48.3	−09 31 43	...	2MASS 05074833−0931432
2MASS 05094864−0906065	05 09 48.6	−09 06 07	G8	(May not be a member of IC 2118; see Kun et al. 2004)
2MASS 05112460−0818320	05 11 24.6	−08 18 32	M0	...

Notes.
[a] From Kun et al. (2004).
[b] Covered only by our MIPS map.
[c] Covered by our IRAC and MIPS maps.
[d] Has a mid-IR excess as determined here via *Spitzer* colors.
[e] Lee et al. (2005) identifies 2MASS 05073016−0610158 as an M0, and 2MASS 05073060−0610597 as an M2.

2. OBSERVATIONS AND DATA REDUCTION

2.1. Spitzer Observations

We observed IC 2118 with *Spitzer* using both IRAC and MIPS. These observations were obtained as director's discretionary time (DDT) as part of the Spitzer Observing Program for Teachers and Students. Most of the data were part of programs 235 and 266 (PI: T. Spuck), obtained in Spring 2005 and 2006, respectively; additional observations of small portions of the map were obtained as part of program 462 (PI: L. Rebull) in Fall 2007 and Spring 2008 in an effort to increase the legacy value of the data set. The IRAC observation was broken into nine astronomical observation requests (AORs), and the MIPS observation into three; the associated AORKEYs[12] are given in Table 2. The IRAC observations used the 12 s high-dynamic-range (HDR) mode such that each exposure consists of a 0.6 s and 12 s frame. There were three dithers per position to minimize instrumental effects, stepping by 260″ for each portion of the map. The IRAC observation covers ∼1.6 deg^2 in all four IRAC bands (3.6, 4.5, 5.8, and 8 μm); Figure 2 shows a three-color IRAC mosaic made using 4.5, 5.8, and 8 μm. The outlines of our MIPS and optical observations are included for reference.

The MIPS observations were fast scans, and each scan leg is offset by 160″ (half an array). There is complete coverage at 70 μm and two scan legs per position at 24 μm. We did not anticipate having viable 160 μm data, so we did not plan on complete coverage at this bandpass. However, the observations were conducted in cold MIPS campaigns, which results in viable data even if the coverage is incomplete. The MIPS observation covers ∼4 deg^2; the 24, 70, and 160 μm full mosaics are shown in Figure 3.

2.2. IRAC Data Reduction

For the IRAC data, we started with the Spitzer Science Center (SSC) pipeline-processed basic calibrated data (BCDs), version S18.7 for program 235 and S18.5 for the two other programs; for our purposes, there is no difference between these pipeline versions. We further processed the BCDs with the IRAC artifact mitigation software written by S. Carey and available on the SSC Web site. Mosaics were constructed from the corrected BCDs using the SSC mosaicking and point source extraction software package MOPEX (Makovoz & Marleau 2005). The mosaics were computed to have a pixel scale of 1.″22 pixel^{-1}.

[12] AORKEYs are the unique 8-digit identifier for the AOR, which can be used to retrieve these data from the Spitzer Archive.

Table 2
Summary of IRAC and MIPS Observations

Program	AORKEY	Map Center	Date Obtained
	IRAC		
235	13375232	5:07:33.00 −6:17:00.0	2005 Mar 25
266	16940288	5:05:52.00 −6:27:52.0	2006 Mar 24
266	16941056	5:03:55.00 −6:42:22.0	2006 Mar 24
266	16941312	5:05:17.00 −7:10:38.0	2006 Mar 23
266	16941568	5:04:24.00 −7:41:48.0	2006 Mar 24
266	16941824	5:03:10.00 −7:04:57.0	2006 Mar 24
462	24248832	5:06:29.50 −6:52:58.1	2008 Mar 09
462	24249088	5:07:18.39 −6:07:11.1	2007 Oct 16
462	24249344	5:07:31.60 −6:21:50.1	2007 Oct 16
	MIPS		
235	13374976	5:07:33.00 −6:17:00.0	2005 Mar 10
266	16940544	5:06:10.00 −6:47.47.0	2006 Mar 31
266	16940800	5:03:42.00 −7:29:19.0	2006 Mar 31

We ran the APEX portion of MOPEX for source detection on the mosaics; we performed aperture photometry on the combined long- and short-exposure mosaics separately using the APEX output and the "aper" IDL procedure from the IDLASTRO library. We used a 2 pixel aperture radius and a sky annulus of 2–6 pixels. The (multiplicative) aperture corrections we used follow the values given in the IRAC Data Handbook: 1.213, 1.234, 1.379, and 1.584 for IRAC channels 1–4, respectively. Flux densities have been converted to magnitudes with the zero magnitude flux densities of 280.9 ± 4.1, 179.7 ± 2.6, 115.0 ± 1.7, and 64.1 ± 0.9 Jy for channels 1–4 respectively, as given in the IRAC Data Handbook.

To make a realistic estimate of the internal uncertainties, we obtained photometry from the individual BCD images for the candidate members. We found that the scatter within that distribution is generally of order 1%. Absolute uncertainties, arising from source variability and uncertainties in the instrument calibration (primary calibrators, aperture corrections, etc.), will be an additional error. This absolute calibration uncertainty is

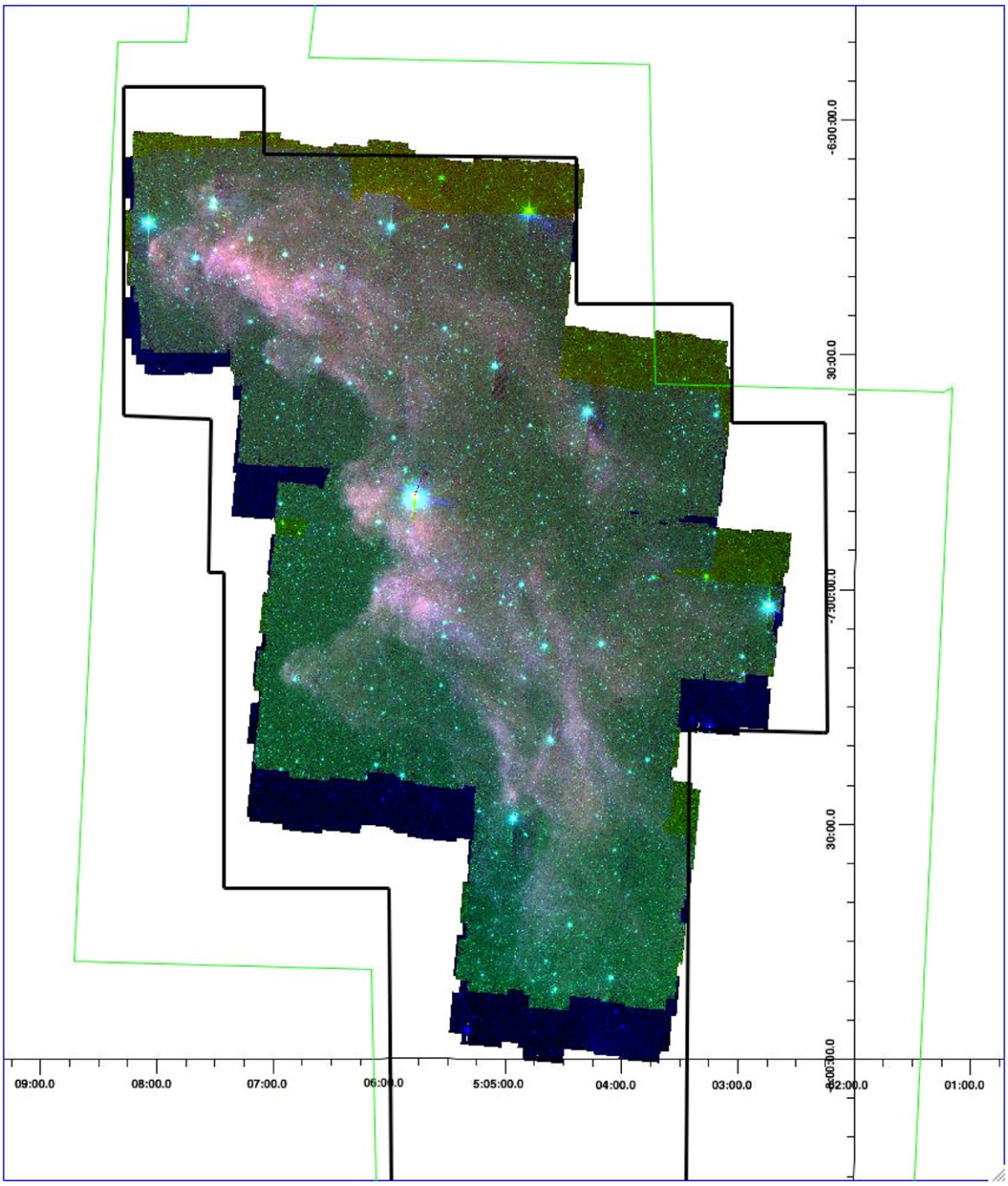

Figure 2. Three-color view of IC 2118 with 3.6 μm in blue, 4.5 μm in green and 8 μm in red. Outlines of our optical (black line) and MIPS (green line) surveys are also plotted.

estimated to be at least ∼1.4%. For the longer integration times, we estimated average photometric errors in the four IRAC channels to be 0.02 mag for bright stars, increasing to 0.1 mag at 17.2, 16.6, 14.4, and 13.8 mag for channels 1–4, respectively.

The APEX source detection algorithm has a tendency to identify multiple sources within the point-spread function (PSF) of a single bright source, which can cause significant confusion at the bandmerging stage. Because our flux densities are determined from aperture photometry with a 2 pixel aperture radius that is not deblended, any object with a companion within 2 pixels is not actually resolved. The photometry lists were therefore purged of multiple sources prior to bandmerging; objects with an accidental companion within 2 pixels had the lower signal-to-noise source removed.

We extracted photometry from the long and short exposure mosaics separately for each channel, and merged these source lists together by position using a search radius of 2 pixels (2.″44) to obtain a catalog for each channel. The magnitude cutoff transition, where we used the long exposure rather than the short exposure photometry, corresponds to magnitudes of 11, 10, 8.4, and 7.5 mag for channels 1 through 4, respectively. We obtained ∼40,000 sources in channel 1, ∼34,000 sources in channel 2, ∼7500 in channel 3, and ∼5000 sources in channel 4. These relative numbers are consistent with expectations from

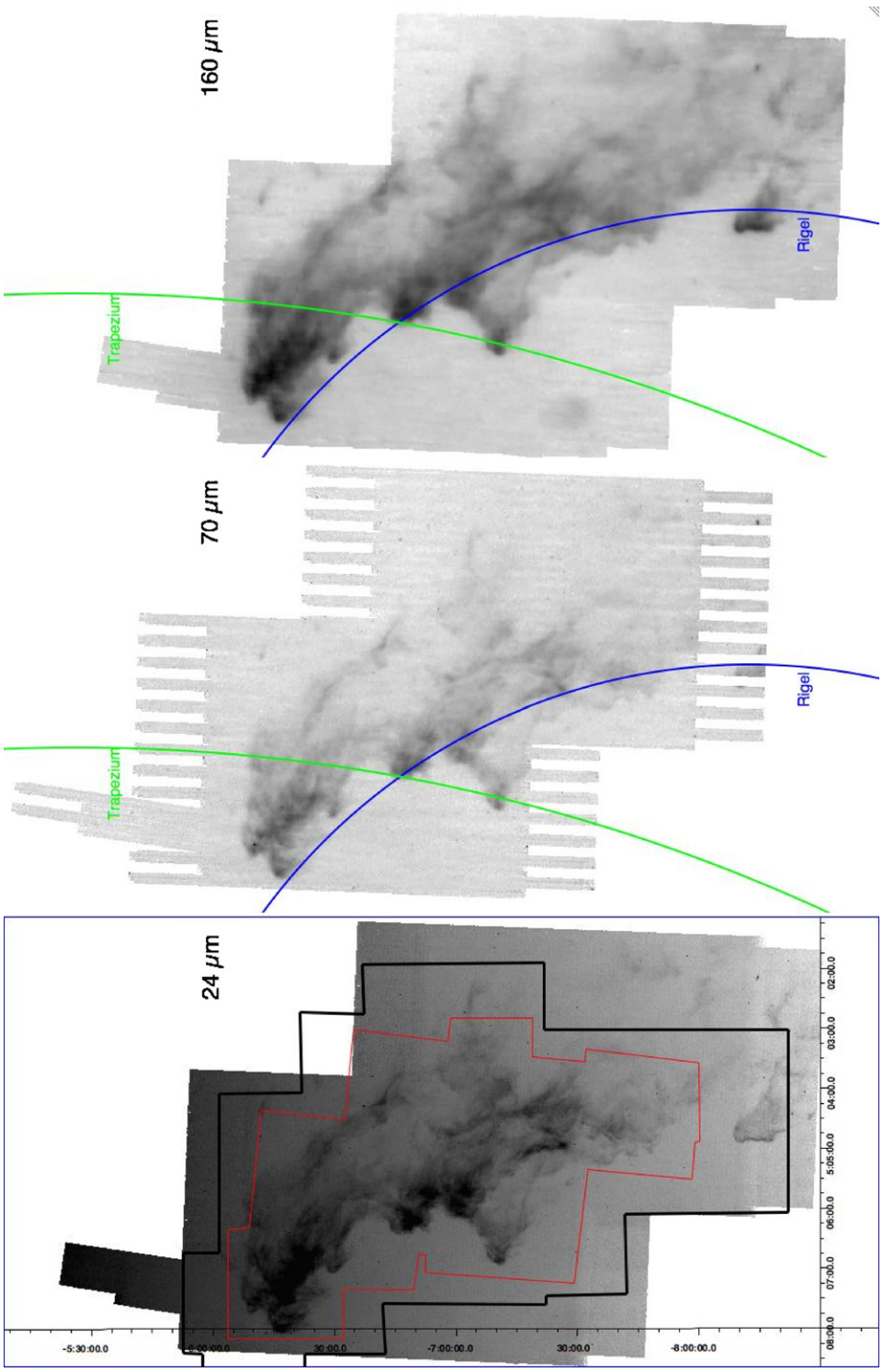

Figure 3. 24 μm, 70 μm, and 160 μm MIPS mosaics of IC 2118. Outlines of our optical (black line) and IRAC (red line) surveys are also included on the 24 μm mosaic. The arcs are from circles that are centered on the Trapezium (green circle, 7.°35 radius) and on Rigel (blue circle, 4.°48 radius).
(A color version of this figure is available in the online journal.)

other star-forming regions and with the sensitivities of the channels.

2.3. MIPS Data Reduction

For MIPS, we started with the SSC-pipeline-produced BCDs, version S16.1. The 24 μm data were processed differently from the 70 and 160 μm data.

For 24 μm, we used MOPEX to construct a mosaic from the BCDs, with the pixel scale set at 2.″45, very close to native pixel size. We used the APEX 1-Frame routines and the point-response function (PRF) provided on the SSC Web site to perform point-source PRF-fitting photometry on the mosaics. We determined via visual inspection that 24 μm sources with an APEX-extracted signal-to-noise ratio (S/N) below 7 were not reliable; therefore, we did not include those sources in the

following analysis. Moreover, we inspected individual sources and removed 13 more clearly false detections (arising from nebulosity or diffraction patterns around bright stars). This resulted in a catalog of 1082 point sources ranging from 0.9 mJy to 700 mJy. The zero point used to convert flux densities to magnitudes is 7.14 Jy, based on the extrapolation from the Vega spectrum as published in the MIPS Data Handbook. We took the error from the S/N returned by APEX as the baseline statistical error. However, the true uncertainty is affected by flat fielding issues, etc., and is estimated to be ∼4%. We added a 4% flux error in quadrature to the APEX-derived error to estimate our final 24 μm uncertainties.

At 70 and 160 μm, the individual unfiltered frames (more than 5400 BCD files) were combined using MOPEX, setting their pixel scales to their native values of 9.″8 and 16″ for 70 and 160 μm, respectively. The final mosaic at 70 μm has a peak surface brightness of ∼100 MJy sr^{-1}, which is within the linear regime of the 70 μm array (Gordon et al. 2007); for the 160 μm mosaic, the value is ∼200 MJy sr^{-1} which is also in the linear regime of the array (Stansberry et al. 2007), and therefore we expect at most a 20% absolute flux density uncertainty. The data were further processed to maintain the structure of the extended emission and preserve its calibration. For the 160 μm mosaic, we applied a two-dimensional (3×3 native pixel) median boxcar filter to interpolate across missing ("NaNs" or "not a number") data due to the incomplete coverage (see above). This step affects only those pixels near the "NaNs" by a few percent. For both Ge channels, we destriped the image using a ridgelet algorithm (J. Ingalls 2009, private communication), which conserves flux and reduces the noise. For the 70 μm point sources, we performed point-source photometry in the same fashion as we did for 24 μm, using APEX 1-Frame on the mosaic constructed as described, and the SSC-provided PRF. Sources with S/N below 8 were rejected, and we carefully removed obvious false detections by individual inspection. This resulted in a catalog of 84 point sources. The zero point used for conversion between flux densities and magnitudes for the 70 μm data is 0.77 Jy, again from the MIPS Data Handbook.

No point sources were detected in the 160 μm data.

2.4. Optical Observations and Data Reduction

We obtained UVR_cI_c images by observing with the United States Naval Observatory (USNO) 40 inch telescope (Flagstaff, AZ) over several epochs between 2006 November and 2007 January. An area of 2.8 deg^2 was covered in all 4 bands by mosaicking the ∼23.′9 × 23.′2 field of view. We acquired at least two images at two different exposure times for each pointing; see Table 3. On 2010 March 15, an additional epoch of relatively short (⩽60 s) integrations was obtained in VR_cI_c just of the head of the nebula (where our YSO candidates are located; see below) as a final check on our measurements. Aperture photometry was performed on the objects in each frame, magnitudes between ∼10 and 12 in the shallowest integrations and ∼20 and 22 in each band in the deepest integrations, subject to variations in the quality of each night. Absolute photometric calibration was achieved through observation of Landolt standards during each night.

The additional epoch in 2010 allowed us to check our calibration and assess intrinsic variability in these stars on ∼3 year timescales. Several of the YSO candidates are variable, some highly variable (>0.2 mag; see Table 4). The three most variable sources are all embedded in reflection nebulae.

In order to include the optical data in our spectral energy distributions (SEDs), we needed to convert the measured magnitudes to flux densities in Janskys. For the U and V filters, we used the Johnson zero points from Allen's Astrophysical Quantities (Arthur 2001), specifically 1823 and 3781 Jy, respectively. For the R_c and I_c filters, we used the zero points from Bessell (1979), which are 3040 and 2433 Jy, respectively.

2.5. Bandmerging

We matched IRAC sources from adjacent channels to empirically estimate our astrometric uncertainty. The histograms of coordinate differences show a 1σ uncertainty of ∼0.″3 in both directions. At this Galactic latitude and longitude (207.4,−27.9), the density of sources is relatively low (∼10 detections per square arcmin in the 3.6 μm images, 4 detections per square arcmin in R_c and I_c images). Via empirical tests across all bands, we determined that a 2″ radius (1.6 IRAC pixels) for source matching works for our sources across the optical, 2MASS, IRAC, and MIPS bands. For a matching radius less than ∼1″, not all of the real matches are found. The number of matches increases steeply with radius until 1″; after that, the number of matches increases slowly with radius until ∼4″ where the number of matches is dominated by false source associations. Using a matching radius of 2″ appears to provide the best possible merging of sources across bands, even for 24 μm; the centroiding for the 24 μm data is much better than 2″, even though the data have a spatial resolution of ∼6″.

Because the 3.6 μm observations are the most sensitive of our *Spitzer* observations, we started by constructing a catalog based on these detections. To be included this catalog, sources have to be detected in 3.6 μm and in at least one of the other bands. Out of the 39,817 sources in this catalog, 3365 (8.5%) have been detected in all 4 IRAC channels, 15% in the JHK_s bands, 50% in the I_c band (recall that the optical observations are deeper than the 2MASS observations), and just 12% in the U band. At 24 μm, 1% (426 sources) of the 3.6 μm-based catalog are detected. However, since the spatial coverage provided by our MIPS map is larger than that for IRAC, and since some very embedded young objects may not be detected in shorter wavelengths than 24 μm, we have also included in the catalog those sources with 24 μm detections even if they do not have 3.6 μm detections. Out of the 1082 sources detected in 24 μm, 48% are detected in the I_c band and 27% in the U band. However, the region mapped by MIPS is not exactly matched to the optical observations; considering just the region covered by both the optical and MIPS maps, these numbers become 69% and 39%, respectively. Similarly, 30% of the 24 μm sources are detected in all four IRAC bands; if one is restricted to the area covered by both MIPS and IRAC maps, 70% are detected at all four IRAC bands plus MIPS-24. Finally, 38% of the 24 μm sources are detected in JHK_s.

3. SELECTION OF YSO CANDIDATES WITH IR EXCESS

With our new multi-wavelength view of the molecular cloud, we can begin to look for the members of this complex. We focus on finding sources having an infrared excess characteristic of YSOs surrounded by a dusty disk. We do not expect to find a dense population of YSOs (see Section 1). Additionally, the molecular cloud is not very dense, so it will not obscure many of the background sources. Thus, we expect a high source contamination rate. Separating the YSO candidates from the extraneous sources requires an extensive weeding-out of the

Table 3
Summary of Our UVR_cI_c Observations from 2006 November–2007 January

No.	R.A. (2000)	Decl. (2000)	U exp. (s)	V exp. (s)	R_c exp. (s)	I_c exp. (s)	U Date	V Date	R_c Date	I_c Date
1	05:08:14.820	−6:16:39.062	1800, 180	900, 60	20, 600	60, 600, 10	2006 Nov 18, 2006 Nov 17	2006 Nov 18, 2006 Nov 17	2006 Nov 17, 2006 Nov 18	2006 Nov 17, 2006 Nov 18, 2006 Nov 17
2	05:08:12.326	−6:16:49.188	900, 180, 360	900, 180, 60, 120, 30	5, 900, 180, 20, 30, 2	20, 30, 2, 5, 900, 180, 60, 600, 10	2006 Oct 31, 2006 Nov 17, 2007 Jan 9	2006 Oct 31, 2006 Oct 31, 2006 Nov 20, 2007 Jan 9, 2006 Nov 21	2006 Oct 31, 2006 Oct 31, 2006 Nov 20, 2006 Oct 31, 2006 Nov 18	2006 Nov 21, 2006 Oct 31, 2006 Nov 18, 2006 Oct 31, 2006 Oct 31, 2006 Oct 31, 2006 Nov 20, 2006 Nov 18, 2006 Nov 21
3	05:08:11.814	−6:04:28.112	1800, 180	900, 60	20, 600	60, 600, 10	2006 Nov 18, 2006 Nov 17	2006 Nov 18, 2006 Nov 17	2006 Nov 17, 2006 Nov 18	2006 Nov 17, 2006 Nov 18, 2006 Nov 17
4	05:06:54.960	−6:13:32.816	180, 600, 360	900, 60, 120	20, 600	60, 600, 10	2006 Nov 17, 2006 Nov 19, 2007 Jan 9	2006 Nov 19, 2006 Nov 17, 2007 Jan 9	2006 Nov 17, 2006 Nov 19	2006 Nov 20, 2006 Nov 19, 2006 Nov 19
5	05:05:35.082	−6:13:31.057	180, 600	900, 60	20, 600	60, 600, 10	2006 Nov 17, 2006 Nov 19	2006 Nov 19, 2006 Nov 17	2006 Nov 17, 2006 Nov 19	2006 Nov 17, 2006 Nov 19, 2006 Nov 19
6	05:06:54.658	−6:33:28.589	180, 600	900, 60	20, 600	60, 600, 10	2006 Nov 17, 2006 Nov 20	2006 Nov 19, 2006 Nov 17	2006 Nov 17, 2006 Nov 19	2006 Nov 19, 2006 Nov 19, 2006 Nov 19
7	05:05:34.572	−6:33:29.144	180, 600	900, 60	20, 600, 40	20, 60, 600, 10	2006 Nov 17, 2006 Nov 21	2006 Nov 21, 2006 Nov 17	2006 Nov 17, 2006 Nov 21, 2007 Jan 9	2007 Jan 9, 2006 Nov 17, 2006 Nov 21, 2006 Nov 17
8	05:04:14.580	−6:33:27.864	180, 600	900, 60	20, 60, 600	60, 600, 10	2006 Nov 17, 2006 Nov 21	2006 Nov 21, 2006 Nov 17	2006 Nov 17, 2006 Nov 21, 2006 Nov 21	2006 Nov 21, 2006 Nov 21, 2006 Nov 17
9	05:07:25.289	−6:48:31.295	180, 600	900, 60	20, 600	60, 600, 10, 2	2006 Nov 17, 2006 Nov 21	2006 Nov 21, 2006 Nov 17	2006 Nov 17, 2006 Nov 21	2006 Nov 21, 2006 Nov 21, 2006 Nov 17, 2006 Nov 21
10	05:06:05.416	−6:48:28.150	180, 600, 360	900, 60, 120	900, 20, 600	15, 900, 60, 600, 10	2006 Nov 17, 2006 Nov 21, 2007 Jan 9	2006 Nov 21, 2006 Nov 17, 2007 Jan 9	2007 Jan 9, 2006 Nov 17, 2007 Jan 19	2007 Jan 9, 2007 Jan 9, 2006 Nov 17, 2007 Jan 19, 2006 Nov 17
11	05:04:47.396	−6:48:48.174	180, 600	900, 60, 600, 10	900, 20, 600, 2	900, 60, 600, 10, 2	2006 Nov 17, 2007 Jan 19	2007 Jan 19, 2006 Nov 17, 2007 Jan 9, 2007 Jan 9	2007 Jan 9, 2006 Nov 17, 2007 Jan 19, 2006 Nov 17	2007 Jan 9, 2006 Nov 17, 2007 Jan 19, 2006 Nov 17, 2006 Nov 17
12	05:03:25.438	−6:48:44.163	180, 600	900, 60, 600	900, 20, 600	900, 60, 600, 10	2006 Nov 20, 2007 Jan 19	2007 Jan 19, 2006 Nov 20, 2007 Jan 9	2007 Jan 9, 2006 Nov 20, 2007 Jan 19	2007 Jan 9, 2006 Nov 20, 2007 Jan 19, 2006 Nov 20

Table 3
(Continued)

No.	R.A. (2000)	Decl. (2000)	U exp. (s)	V exp. (s)	R_c exp. (s)	I_c exp. (s)	U Date	V Date	R_c Date	I_c Date
13	05:07:24.998	−7:08:25.470	1800, 180	900, 60	20, 600	60, 600, 10	2006 Nov 20, 2006 Nov 20	2006 Nov 20, 2006 Nov 20	2006 Nov 20, 2006 Nov 20	2006 Nov 20, 2006 Nov 20, 2006 Nov 20
14	05:06:07.763	−7:08:48.399	180, 600	900, 60, 10	20, 600, 10	15, 60, 600, 10	2006 Nov 20, 2007 Mar 20	2007 Mar 20, 2006 Nov 20, 2006 Nov 20	2006 Nov 20, 2007 Mar 20, 2006 Nov 20	2007 Jan 15, 2006 Nov 20, 2007 Mar 20, 2006 Nov 20
15	05:04:48.979	−7:09:27.985	180, 600	900, 60, 30, 10	20, 600, 2	60, 600, 10, 2	2006 Nov 20, 2007 Feb 15	2007 Feb 15, 2006 Nov 20, 2006 Nov 20, 2006 Nov 20	2006 Nov 20, 2007 Feb 15, 2006 Nov 20	2006 Nov 20, 2007 Feb 15, 2006 Nov 20, 2006 Nov 20
16	05:03:24.572	−7:08:17.494	180, 600	3, 900, 60, 30	20, 600, 2	60, 600, 10, 2	2006 Nov 20, 2007 Feb 15	2006 Nov 20, 2007 Feb 15, 2006 Nov 20, 2006 Nov 20	2006 Nov 20, 2007 Feb 15, 2006 Nov 20	2006 Nov 20, 2007 Feb 15, 2006 Nov 20, 2006 Nov 20
17	05:07:18.477	−7:28:30.082	600	900, 60, 30	20, 60, 600	60, 600, 10	2007 Mar 18	2007 Mar 18, 2006 Nov 20, 2006 Nov 20	2006 Nov 20, 2006 Nov 20, 2007 Mar 18	2006 Nov 20, 2007 Mar 18, 2006 Nov 20
18	05:06:00.376	−7:28:55.094	180, 600	900, 60, 30	20, 600, 10	60, 600, 10, 2	2006 Nov 20, 2007 Mar 19	2007 Mar 19, 2006 Nov 20, 2006 Nov 20	2006 Nov 20, 2007 Mar 19, 2006 Nov 20	2006 Nov 20, 2007 Mar 19, 2006 Nov 20, 2006 Nov 20
19	05:04:36.463	−7:29:11.645	180, 600	900, 60, 600	20, 600	60, 600, 10, 2	2006 Nov 20, 2007 Mar 17	2007 Mar 17, 2006 Nov 20, 2007 Jan 17	2006 Nov 20, 2007 Mar 17	2006 Nov 20, 2007 Mar 17, 2006 Nov 20, 2006 Nov 20
20	05:05:57.436	−7:48:33.482	180, 600	900, 60, 30	20, 600, 10	60, 600, 10, 2	2006 Nov 20, 2007 Jan 18	2007 Jan 18, 2006 Nov 20, 2006 Nov 20	2006 Nov 20, 2007 Jan 18, 2006 Nov 20	2006 Nov 20, 2007 Jan 18, 2006 Nov 20, 2006 Nov 20
21	05:04:37.303	−7:48:37.014	600	900, 60, 30	20, 600	60, 600, 10	2007 Jan 18	2007 Jan 18, 2006 Nov 20, 2006 Nov 20	2006 Nov 20, 2007 Jan 18	2006 Nov 20, 2007 Jan 18, 2006 Nov 20
22	05:05:55.785	−8:08:07.414	180, 600	900, 60, 10	20, 600, 2	5, 60, 600, 10, 2	2006 Nov 21, 2007 Jan 18	2007 Jan 18, 2006 Nov 21, 2006 Nov 21	2006 Nov 21, 2007 Jan 18, 2006 Nov 21	2006 Nov 21, 2006 Nov 21, 2007 Jan 18, 2006 Nov 21, 2006 Nov 21
23	05:04:32.104	−8:09:00.677	180, 600	900, 60, 10	20, 600, 2	60, 600, 10, 2	2006 Nov 21, 2007 Jan 18	2007 Jan 18, 2006 Nov 21, 2006 Nov 21	2006 Nov 21, 2007 Jan 18, 2006 Nov 21	2006 Nov 21, 2007 Jan 18, 2006 Nov 21, 2006 Nov 21

Table 4
Measured Magnitudes for *Spitzer*-selected YSO Candidates in IC 2118[a]

SST Name	2MASS Name	U	σ	V	R_c	I_c	J	σ	H	σ	K_s	σ	[3.6]	[4.5]	[5.8]	[8.0]	[24]	[70]	σ
050650.1–061908	05065009–0619079	...	...	21.59	19.35	17.43	13.30	0.027	12.16	0.026	11.53	0.025	10.75	10.38	10.04	9.52	6.79	...	...
050653.5–061712[b]	05065349–0617123	20.99	0.102	17.00	15.20	13.71	11.16	0.026	9.91	0.027	9.13	0.024	8.20	7.76	7.31	6.51	3.27	0.53	0.044
050711.6–061510[b,c]	05071157–0615098	18.91	0.033	16.29	15.01	13.85	13.02	0.026	11.28	0.027	10.02	0.029	8.74	8.11	7.63	7.07	4.78	...	...
050720.6–061612	05072058–0616119	21.93	0.225	19.50	17.58	15.47	12.91	0.020	12.07	0.021	11.63	0.021	10.82	10.30	9.86	9.13	6.42	...	...
050721.9–061152	05072188–0611524	...	...	19.36	18.04	16.88	15.04	0.043	13.99	0.045	13.28	0.030	12.27	11.67	11.36	11.15	5.45	0.80	0.058
050728.7–061326	05072865–0613258	20.29	0.058	18.32	16.68	14.81	12.50	0.028	11.52	0.030	11.04	0.024	10.57	10.17	9.87	9.25	6.19	...	...
050729.4–061637	05072937–0616368	21.43	0.152	19.03	17.55	16.10	13.71	0.023	12.41	0.024	11.54	0.019	10.27	9.44	8.80	7.63	4.33	...	...
050730.2–061016[b,c]	05073016–0610158	17.10	0.030	14.99	13.72	12.54	10.82	0.023	9.57	0.027	8.61	0.019	7.30	6.77	6.35	5.55	2.43	−0.39	0.030
050730.6–061060[b,c]	05073060–0610597	17.58	0.030	14.74	13.47	12.21	10.12	0.025	9.04	0.029	8.25	0.015	7.40	7.02	6.70	6.13	3.41	1.20	0.103
050733.7–061348	05073372–0613474	20.74	0.080	19.19	17.41	15.39	13.01	0.020	12.39	0.026	12.02	0.019	11.40	10.92	10.55	9.71	7.08	...	...

Notes.
[a] The errors in the VRI_c, IRAC, and MIPS-24 data are dominated by systematic errors; they are 0.03–0.05, 0.05, and 0.04 mag, respectively (see the text).
[b] Previously identified YSO; see Table 1.
[c] Nebulous and highly variable (>0.2 mag) in the optical in our observations.

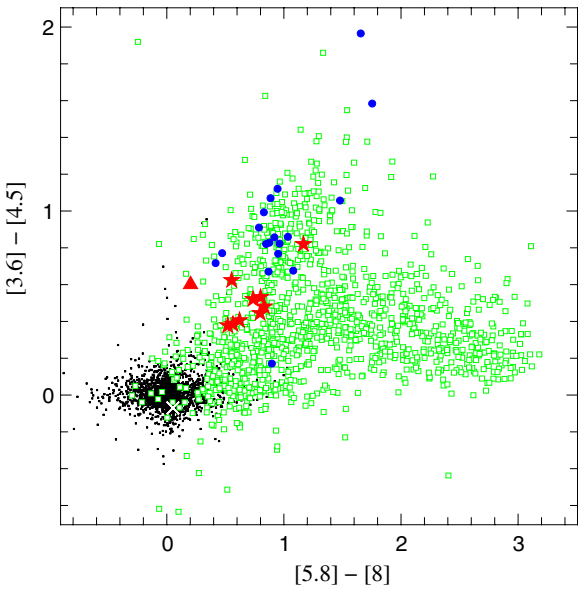

Figure 4. [3.6] − [4.5] vs. [5.8] − [8] color–color diagram. Sources flagged as PAH emission sources (background galaxies) or AGN by our selection method are plotted in green squares. Red star symbols are selected YSOs candidates with [3.6] < 12 and blue points are YSO candidates selected in the same fashion but with [3.6] > 12. The red triangle is an edge-on disk candidate (see Section 3.2). The black points are the remaining detections. The × symbol near zero color is the weak-lined T Tauri (wTTS) candidate (2MASS J05060574−0646151, see Section 4.2). See the text for more discussion of each of these categories.

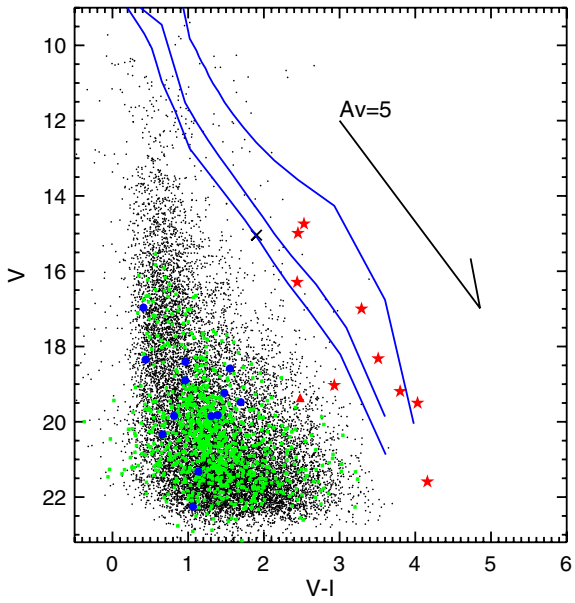

Figure 5. Optical V vs. $V - I_c$ color–magnitude diagram. The symbols are the same as in Figure 4. Note that the blue dots representing the [3.6] > 12 sources are in fact plotted, but they are in amongst the green squares and black dots well below the zero-age main sequence (ZAMS); this we take to be further evidence that the objects represented by the blue dots are contaminants and not YSO candidates. The red triangle is the edge-on disk candidate, which appears here below the ZAMS, as appropriate for such an object. The solid blue lines are models from Siess et al. (2000) at 1, 10, and 30 Myr and scaled to 210 pc, where we have tuned the color-effective temperature relation such that the 100 Myr isochrone matches that of the Pleiades single-star sequence (Stauffer et al. 2007; Jeffries et al. 2007). A reddening vector is also indicated.

galactic and extragalactic contaminants. To begin this task, we identify objects with excesses at IRAC and MIPS wavelengths. Then, we use filtering mechanisms from the literature based on *Spitzer* colors to distinguish likely galaxies from likely members. We also use the additional information we have from the optical to further winnow the candidate list.

3.1. IRAC Selection

We first select sources using a set of IRAC color–magnitude and color–color diagrams. Our selection is based on the Gutermuth et al. (2008) method and is described in Guieu et al. (2009); in summary, this method uses cuts in several IRAC color–color and color–magnitude spaces to identify likely YSOs and likely contaminants such as active galactic nuclei (AGNs). Using this technique, we identified 459 sources having colors consistent with galaxies dominated by polycyclic aromatic hydrocarbon (PAH) emission and 765 more sources having colors consistent with AGN. Just 27 sources are not flagged as background contaminants and have colors compatible with YSOs with an IRAC excess in the [3.6]−[5.8]/[4.5]−[8] plane (where the bracket notation denotes magnitudes, e.g., [3.6] means magnitude at 3.6 μm). Figure 4 shows the IRAC color–color diagram for the sources that passed and failed these color tests. (We note for completeness that Gutermuth et al. 2009 have updated their YSO selection method with new rejection criteria; we have verified that these new criteria do not affect our list of YSO candidates.)

Since we expect to find a lot of contamination here, the list of 27 sources not flagged as contaminants bears further scrutiny. These 27 sources consist of 9 sources brighter than [3.6] = 12, with the remaining 18 all fainter than this limit. The *Spitzer* Wide-area Infrared Extragalactic Survey (SWIRE; Lonsdale et al. 2003) observations of the ELAIS N1 extragalactic field[13] consists of integrations of similar depth, but this sample is expected to be essentially entirely galaxies and foreground stars, and as such provides a guide to the range of values expected from these contaminants. The SWIRE survey shows that very few galaxies have [3.6] brighter than 12 mag. The IC 2118 objects that we have identified explicitly as contaminants have 3.6 μm flux densities comparable to the SWIRE contaminants, with [3.6] ranging from 12 to 18 mag. But, out of the YSO candidates, 18 also have magnitudes fainter than [3.6] = 12. As the brightness decreases, the chances of these objects being background contaminants increases.

Since we have a wealth of supporting data, we can use these data to additionally constrain our YSO selection. Figure 5 shows an optical color–magnitude diagram for these sources. The optical colors and magnitudes for these 18 faint sources all fall in the region occupied by main-sequence stars or background galaxies. In contrast, the 9 remaining YSO candidates with [3.6] < 12 all appear redder, near or above a 30 Myr Siess et al. (2000) isochrone in the $V/V - I_c$ color–magnitude diagram. We strongly suspect that the faint ones are contaminants. The 9 brighter objects selected in [3.6] − [5.8]/[4.5] − [8] with [3.6] < 12 are included in our list of IRAC-selected YSO candidates. For reference, the 18 objects with [3.6] > 12 are represented with a blue filled circle in most of the remaining figures in this paper. The restriction we have imposed that [3.6] < 12 means that we are effectively sensitive to masses greater than 0.1 $M_\odot$ at a distance of 210 pc for an assumed age of ∼3–5 Myr.

All of these nine IRAC-selected YSO candidates are seen at MIPS-24. This is in contrast to the catalog as a whole, where only 10% of the sources seen in all four IRAC bands are also seen at 24 μm. Since legitimate members of IC 2118 with infrared

[13] VizieR Online Data Catalog, II/255 (Surace et al. 2004).

excesses located at ∼210 parsec should be detected at 24 μm by our observations, the fact that we see these objects gives us further confidence that these objects are truly YSOs. Three of them are also seen at 70 μm; similarly, legitimate YSOs with large excesses should be detected by our shallow 70 μm observations, so this also suggests that these objects are true YSOs. (Note, of course, that most of the sources seen in our observations at 24 or 70 μm are foreground stars or background galaxies, so detection at any MIPS band by itself is insufficient evidence for youth.)

We extracted and examined the POSS, 2MASS, and our optical images for each of these candidates to verify that they did not appear extended in any of these bands.[14] While all extended objects may not be galaxies (many YSOs in Taurus at 140 pc appear as extended objects due to circumstellar reflection nebulae, edge-on disks, jets, etc.; see Rebull et al. 2010), extended objects seen here are much more likely to be galaxies than YSOs at 210 pc. All of our YSO candidates passed this check and appear to be point sources in all available bands.

3.2. MIPS Selection

This IRAC-based selection method does not allow us to detect young stars having an infrared excess only at wavelengths longer than 8 μm. We looked for potential sources with a [3.6] − [24] color excess but no IRAC excess, which would be intermediate between photospheric objects and Class II stars; these objects are Class III sources with weak excesses (possible transitional disks). Figure 6 shows the [3.6]/[3.6] − [24] color–magnitude diagram. In this parameter space, photospheres have zero color, and galaxies are red and faint. This figure also contains data from the SWIRE ELAIS N1 field. We have truncated the SWIRE catalog to fit our shallower IC 2118 24 μm detection limit, rejecting SWIRE sources with [24] > 9.4, and plotted the catalog here as black contours. The SWIRE sample is essentially entirely galaxies and foreground stars, and as such provides a visual guide to the locations where such objects appear in the diagram.

The most striking thing about this diagram for IC 2118 is that there are three distinct groups of objects: objects of zero color (likely foreground/background stars), objects that are faint and red (likely galaxies), and objects that are bright and red (likely YSOs). No sources appear between the photospheric/Class III objects and the Class II objects. The bright objects we selected above based on IRAC colors are also bright here, strongly suggesting the presence of an infrared excess we interpret as circumstellar dust. The contaminants identified above are also identified as likely contaminants here; these objects nearly all fall on top of the SWIRE contours. The objects identified as having YSO-like IRAC colors but being as faint as the contaminants are also faint and have contaminant-like colors in this parameter space. Within the faint contaminant portion of the diagram, the YSO candidates are among the brightest or reddest objects, which is a likely result of our selection process. This lends further support to our assertion that the faint objects are likely background galaxies.

Despite the fact that Figure 6 does not reveal any new candidate YSOs near the IRAC-identified candidate YSOs, it does identify another source of particular interest. Figure 6 highlights a source (as a red triangle) that is red, with a [3.6] − [24] color of ∼6.5 and a moderately faint [3.6] ∼ 12, which is among the brighter values for the likely contaminants. This source (named 050721.9−061152) has not strictly been selected as a YSO candidate or background contaminant by our IRAC-based method, but it is located in the border of our YSO selection area in the [3.6] − [5.8]/[4.5] − [8] diagram; it has a clear [3.6] − [5.8] excess but a low [4.5] − [8] excess. Somewhat surprisingly, it is clearly detected at 70 μm. Since our 70 μm survey is shallow enough that we would only detect IC 2118 YSOs if they have a large infrared excess, we take that detection, plus the marginal shorter-band color selections, as evidence that this object may very well be a YSO candidate, and we add it to our list. We discuss this object again below.

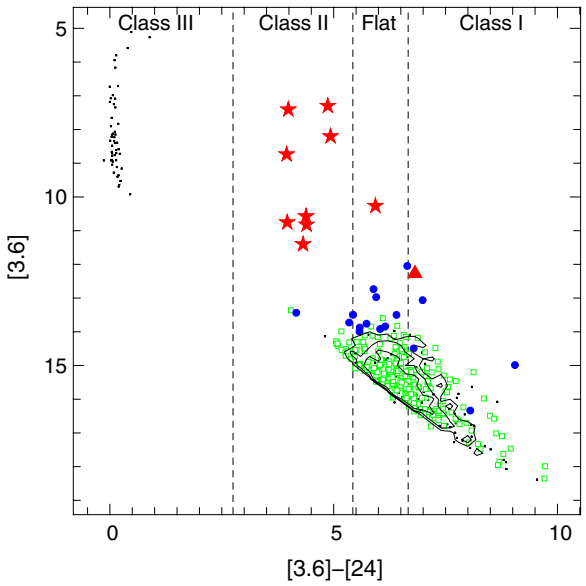

Figure 6. [3.6]/[3.6] − [24] color–magnitude diagram. Symbols are the same as in Figure 4. The black curves are contours from the SWIRE catalog truncated to our IC 2118 detection limit (i.e., [24] < 9.4); see the text.

(A color version of this figure is available in the online journal.)

We use [3.6] versus [3.6] − [24] to look for YSOs, whereas many papers in the literature (e.g., Rebull et al. 2010, and references therein) use the K_s versus K_s − [24] color–magnitude space to find YSOs. In that diagram, the K_s − [24] colors for M stars deviate significantly from zero (Gautier et al. 2007), so objects without disks but with a (possibly unknown) M spectral type will appear to have an infrared excess. The color departure from 0 for M stars using [3.6] − [24] happens at later types than for K_s − [24], which makes it a better choice to use for searches for small excesses in cases where the spectral type of the candidates is unknown. However, one can obviously only construct a [3.6] versus [3.6] − [24] diagram for those regions where one has both IRAC and MIPS data. Since our maps do not match exactly, and since there are previously identified T Tauris well off of the densest parts of the nebula, we also constructed a K_s versus K_s − [24] color–magnitude diagram using 2MASS and MIPS data to see if any YSO candidates appeared off the edge of our IRAC maps. Two new sources appear as potential YSOs here, but by inspection of the images, both of these sources are extended, and one (2MASX J05015386−0745321) is a known galaxy. We do not include either of these objects on our YSO candidate list.

[14] Some of our high school students, trained in observational techniques using the Sloan Digital Sky Survey Galaxy Zoo, participated in this classification. At least three different individuals examined images of each of more than 400 candidates selected by a variety of *Spitzer* color selection mechanisms in order to identify likely galaxies.

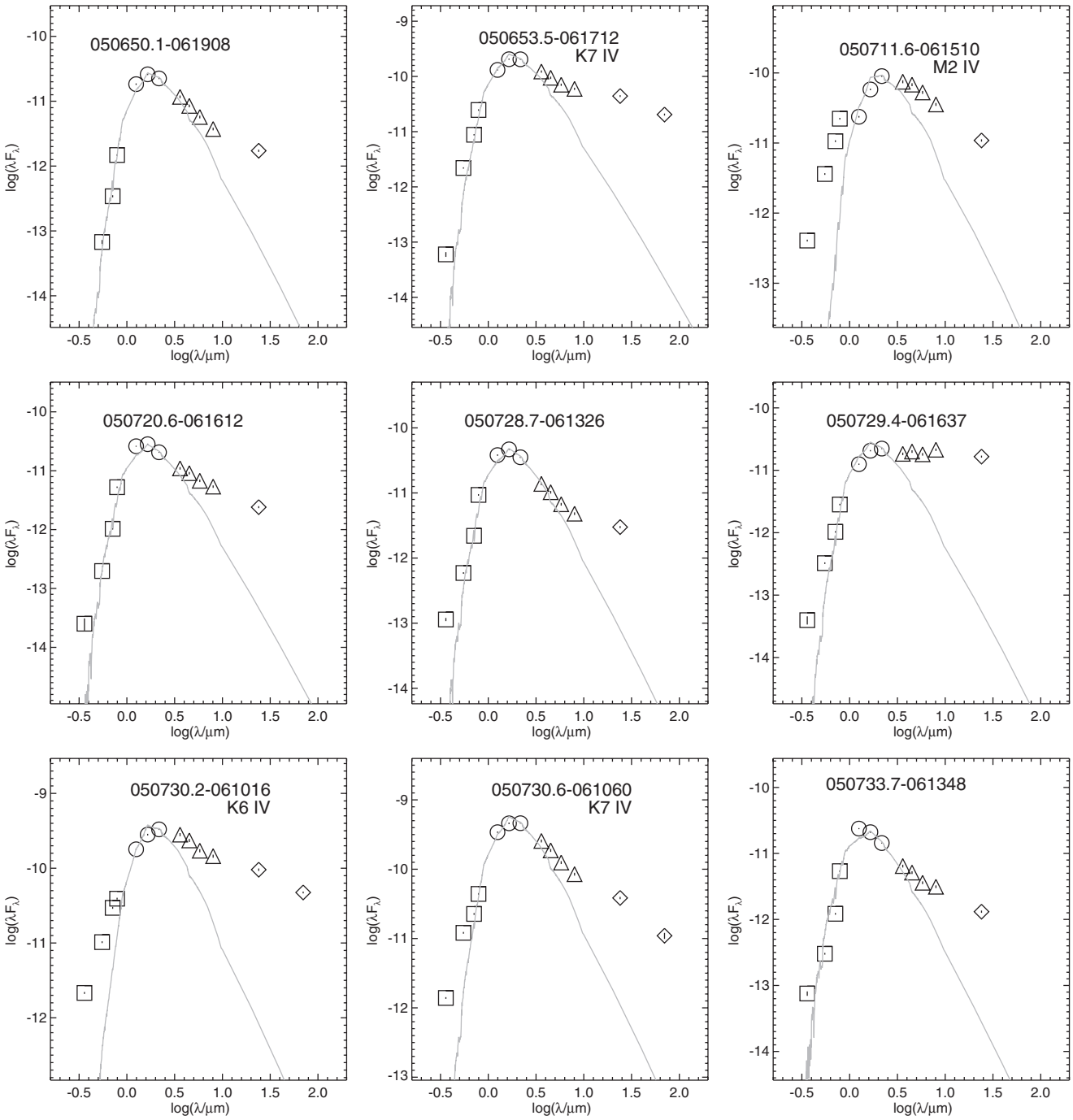

Figure 7. SEDs for nine of our YSO candidates; the 10th is in Figure 8. The squares are our optical points, the circles are 2MASS, the triangles are IRAC, and the diamonds are MIPS. Error bars are indicated, and in most cases are smaller than the symbol. Spectral types are known for some objects from Kun et al. (2004), and those are indicated where possible. In cases where no type is known, an M0 is assumed. Reddened models from the Kurucz–Lejeune model grid (Lejeune et al. 1997, 1998) are shown for reference; see the text.

One previously identified T Tauri star (RXJ 0502.4−0744) is located in our MIPS map but not in the IRAC map, and is detected at 24 μm; however this object does not show $K_s - [24]$ infrared excess. Its measured flux density is 1.3 ± 0.12 mJy at 24 μm ($[24] = 9.36 \pm 0.1$).

4. PROPERTIES OF THE YSO CANDIDATES

4.1. Magnitudes and Spectral Energy Distributions

Coordinates and our measured magnitudes between U and 70 μm for our 10 YSO candidates appear in Table 4. Errors in the optical photometry for these 10 objects are generally dominated by the systematic errors, and as such are essentially all ∼0.1 mag at U, 0.03–0.05 mag at V, R_c, and I_c, 0.02–0.03 mag at JHK_s (where these values come from 2MASS), and 0.02 mag at all four IRAC bands. The 24 μm errors are typically 0.04 mag; the 70 μm errors vary enough between objects that they appear separately in the table. SEDs for the nine IRAC-selected YSO candidates appear in Figure 7. To guide the eye, we wished to add reddened stellar models to these plots, but spectral types are only known for four of the nine candidates. In order to provide a reference, for the remaining objects, we assumed an

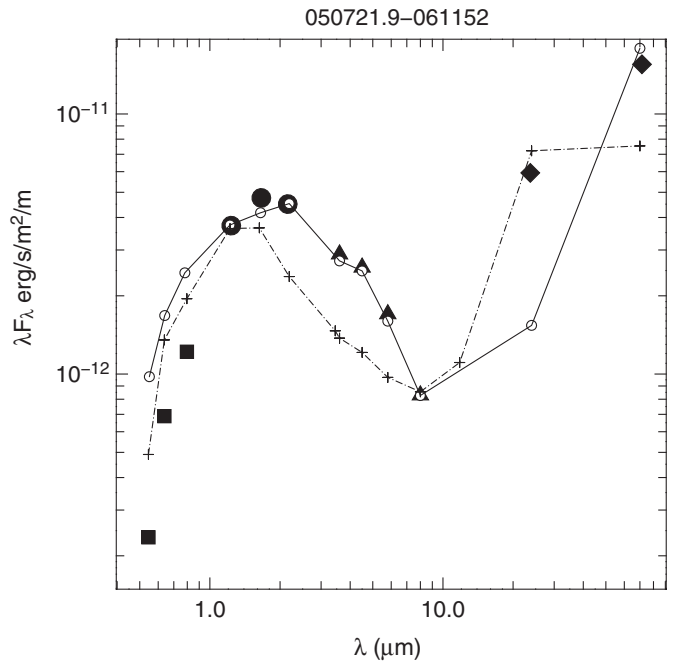

Figure 8. SED of 050721.9−061152 (black filled symbols), compared to the well known edge-on disks HH 30 (solid line, circles; Burrows et al. 1996) and HV Tau C (dashed line, plus symbol; Duchene et al. 2010). These SEDs have been normalized to 050721.9−061152 in the *J* band. For the black filled points, the symbols are as in the previous figure—squares are our optical points, the circles are 2MASS, the triangles are IRAC, the diamonds are MIPS, and the error bars are smaller than the points.

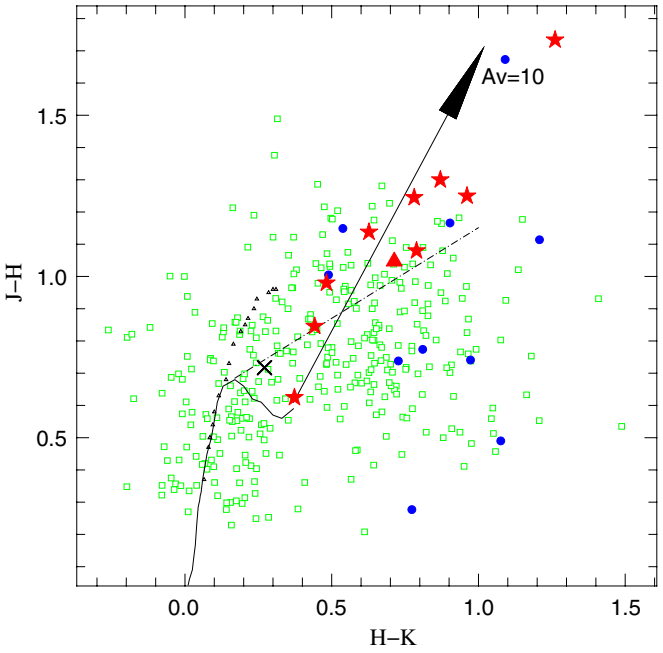

Figure 9. $J - H$ vs. $H - K_s$ diagram for the sample, with the same notation as earlier figures. The T Tauri locus is also indicated (dash-dot line), as is a reddening vector (the arrow). The main sequence is drawn by a solid line and the giant branch by small black triangles. The × symbol is the wTTS candidate (2MASS J05060574−0646151, see Section 4.2). This diagram shows that all but one of the YSOs have an infrared excess starting at *H* band and that they have moderate reddening.

(A color version of this figure is available in the online journal.)

M0 type. Thus, for each object in Figure 7, a reddened model is shown, selected from the Kurucz–Lejeune model grid (Lejeune et al. 1997, 1998) and normalized to *H* band. Note that this is not meant to be a robust fit to the object, but rather a representative stellar SED to guide the eye such that infrared excesses are immediately apparent.

Our 10th YSO candidate is the MIPS-selected object, 050721.9−061152. This object's SED appears in Figure 8 and shows that the strong infrared excess starts after ∼8 μm (which is why this object is not found via the IRAC-based selection method). This kind of SED is typical of a YSO seen edge-on. At wavelengths shorter than ∼24 μm, the thermal emission is absorbed by the disk itself and the source is mostly seen in scattered light; this object is indicated by the the triangles in Figure 5, where it is below the pre-main-sequence locus defined by the other members. At longer wavelengths, the disk becomes optically thin and the thermal emission dominates the SED. In Figure 8, we have compared the SED of 050721.9−061152 with two well-known edge-on disk SEDs: HH 30 (Burrows et al. 1996) and HV Tau C (Duchene et al. 2010). The flux densities have been normalized to match that of 050721.9−061152 in the *J* band. The figure illustrates that the global shape of the 050721.9−061152 SED, with a minimum at 8 μm, is compatible with an edge-on disk YSO. In our color–magnitude (Figures 5, 10, and 6) and color–color (Figures 4 and 9) diagrams, this source is plotted with a red triangle. Its location in the optical CMDs excludes its identification as simply a debris disk or transition disk. Since photospheric optical and NIR emissions are seen through the disk in scattered light, they are hard to predict and broadband observations cannot tell us much about the nature of the central object. If it is an edge-on disk, then it joins a relatively short list of similar objects; such objects can tell us much about the physical properties of the occulting edge-on disk. Further study of this object is warranted.

Out of our entire list of 10 YSO candidates, six are new discoveries. Four of our candidates are already known as young members of IC 2118; they were discovered by Kun et al. (2001, 2004) as classical T Tauri stars (cTTS) using Hα objective prism plates and confirmed by spectroscopy to be young. They are 050711.6−061510, 050653.5−061712, 050730.6−061060, and 050730.2−061016. For one of these, 050711.6−061510, the SED appears "disjoint" between the I_c- and *J*-band observations; this is not uncommon in T Tauri stars, and is usually explained by the star having undergone significant variation in between the epochs of observations. In fact, this star is one of three that appear in our optical observations to be nebulous and highly variable (>0.2 mag) even within the timescale of our observations.

In the spirit of the Lada (1987) and Wilking et al. (2001) Class I/Flat/II/III system, we fit a line to all of the available data between 3.6 to 24 μm. Eight of the IRAC-bright YSO candidates are Class II T Tauri stars and one (050729.4−061637) is a flat disk. These classifications did not change if we instead fit just 3.6 to 8 μm. We did not attempt a similar fit of the edge-on-disk candidate, since the object is seen through the disk, and the slope changes significantly depending on whether the MIPS points are included in the fit.

Since spectral types are not known for six of the ten YSO candidates, it is not easy to determine masses, ages, or degree of reddening. However, Figure 9 shows the $J - H$ versus $H - K_s$ diagram for the sample, with the same notation as earlier figures. By comparison to the ZAMS, it can be seen that all have moderate reddening. The source that does not show significant IR excess in the $J - H$ versus $H - K_s$ diagram is located on

the 1 Myr model isochrone. Likewise in the H versus $H - K_s$ diagram, Figure 10, the T Tauri stars appear well separated from the main sequence stars and the identified background contaminants. They all appear redder than the 1 Myr isochrone model mostly because they have infrared excess starting at H band. If one makes the simplifying and probably incorrect assumption that the offset is entirely due to A_v, and trace the objects back to the 1 or 3 Myr isochrone, the brightest objects are $\sim$2 $M_\odot$, and the faintest are $\sim$0.1 $M_\odot$.

4.2. Previously Identified YSOs Not Recovered by Our Selection

We note that Kun et al. (2004) reported other classical T Tauri star (cTTS) candidates in this region (see Table 1), but they are either on the southern end of the molecular cloud or significantly off the nebular region, and are not covered by our survey.

Kun et al. (2004) reported a weak line T Tauri star (wTTS) candidate (2MASS J05060574−0646151) that may or may not be a true member of IC 2118. This object is within our surveyed region. This object does not show any infrared excess in the IRAC bands and is not detected at any of the MIPS bands. Therefore, our selection methods based on infrared excesses will not recover it. However, its position in our $R_c/R_c - I_c$ and $V/V - I_c$ CMDs is compatible with a pre-main-sequence star according to models and the position of our nine (IRAC-selected) YSOs in the same diagram. This object is represented with a × symbol in optical and NIR color–color and color–magnitude diagrams (Figures 5, 9, 10) and in Figure 11.

4.3. Location of the YSO Candidates

All 10 of our YSO candidates, including the edge-on-disk candidate, are located in the head of the nebula, i.e., G206.4-26.0, the most massive molecular cloud (Kun et al. 2001) of IC 2118. Figure 11 shows the spatial distribution of the YSOs, using the same notation as in earlier figures. The distributions seen here lend further support to our assertions above that the green points are the contaminants (which are evenly distributed), the blue points (faint IRAC-selected objects) are likely galaxies (generally off-cloud and evenly distributed), and the IRAC- and MIPS-selected bright objects are likely YSOs. We expected to find YSO candidates further south in this cloud; however, evidently the conditions do not support substantial star formation in regions other than the "head." The surface brightness of the ISM at 8, 24, 70, and 160 μm is fainter in the southern portion of the nebula compared to the more northern portion. The CO maps from Kun et al. (2001) find that the head of the nebula, G206.4-26.0, at 85 $M_\odot$, is at least 3 times more massive than any of the other clouds. G206.8-26.5, with 28 $M_\odot$, houses only 2MASS J05060574−0646151, the wTTS candidate mentioned in the prior section, which may or may not be a true member of the cloud and does not have an infrared excess. At 24 μm, the peak surface brightness of G206.4-26.0 is $\sim$34 MJy sr^{-1}, and the peak surface brightness of G206.8-26.5 is not that different at $\sim$33 MJy sr^{-1}. At 160 μm, the peak surface brightnesses are $\sim$205 and $\sim$125 MJy sr^{-1}, respectively. The remaining clouds within our map, G207.3-26.5, G207.2-27.1, and G208.1-27.5, are 2, 2, and 6 $M_\odot$, respectively. Kun et al. (2001) find them all to be fainter, cooler, and physically smaller on the sky than either of the other two clouds in the head of the nebula. At 24 μm, their peak surface brightnesses are $\sim$31, $\sim$31, and $\sim$27 MJy sr^{-1}, respectively; at 160 μm, the peaks are $\sim$77, $\sim$30, $\sim$80 MJy sr^{-1}, respectively. All of this suggests that the local conditions are different enough to significantly affect star formation in the two locations.

4.4. Ultraviolet Excesses

Ultraviolet (UV) excesses can also be an indication of youth (see, e.g., Rebull et al. 2000, and references therein). We have U-band measurements for nine of the known plus new candidate IC 2118 members, including the WTTS; the two objects without U measurements are 050721.9−061152 and 050650.1−061908 (see Table 4). Because these objects are subject to moderate reddening, which will significantly affect the U-band observations, a robust determination of the UV excess requires a spectral type and secure determination of A_v. However, the photospheres plotted to guide the eye in Figure 7 suggest that there are UV excesses in at least six of our nine IRAC-selected YSO candidates. Two of the largest apparent UV excesses are in two of the stars with known types, 050730.2−061016 and 050730.6−061060 (omitting 050711.6−061510 because of the evident stellar variation), suggesting that, when better spectral types are obtained for the remaining objects, UV excesses may be apparent in most of them.

4.5. On the Distance to IC 2118

At least two (perhaps) intertwined mysteries enshroud the Witch Head—its distance and the external source responsible for sculpting its surface, illuminating it, and possibly triggering star formation within it. There is at least a factor of two uncertainty in the distance to IC 2118: 210 pc versus 440 pc. Our process for identifying YSOs toward IC 2118 does not depend strongly on the distance; the same stars would have been selected for any distance up to the point where the faintest objects start to blend with the background galaxies, and all of our YSOs are considerably brighter than this limit. However, physical interpretation of the IC 2118 YSOs depends on accurate determination of the distance. For that reason, we return to the distance question now.

Two sources (at different distances) are listed as potential illumination and/or wind-sculpting sources for the nebula—the Trapezium and Rigel. Figure 3 includes two arcs from circles centered on the Trapezium (7.°35 from IC 2118) and Rigel (4.°48 from IC 2118). We discuss these more below.

4.5.1. Arguments in Favor of $d \sim 400$ pc

The most secure and accurate distance for any part of the Orion complex is the distance derived using the VLBA for several members of the Orion Nebula Cluster (ONC) by Menten et al. (2007), which is $d = 414 \pm 7$ pc. As the most massive members of the ONC, we assume that the Trapezium cluster stars, and in particular θ^1 Ori C, are at this distance. Presumably, this also means that the Orion Nebula is at this distance. At slightly lower accuracy, the BN/KL complex just north of the Trapezium has been determined to be at 437 ± 19 pc via VLBI measurement of water masers. This puts the most active current star formation and the densest molecular gas in Orion at $\geqslant$400 pc.

As noted by Bally et al. (1991) and expanded upon considerably by Ogura & Sugitani (1998, hereafter OS98), there is a large population of nebular structures surrounding the ONC, many of which have cometary shapes or other morphology suggestive of shaping by winds or UV photoionization. If arrows are attached to each structure pointing toward the apparent direction of the wind, these arrows form a centro-symmetric pattern pointing

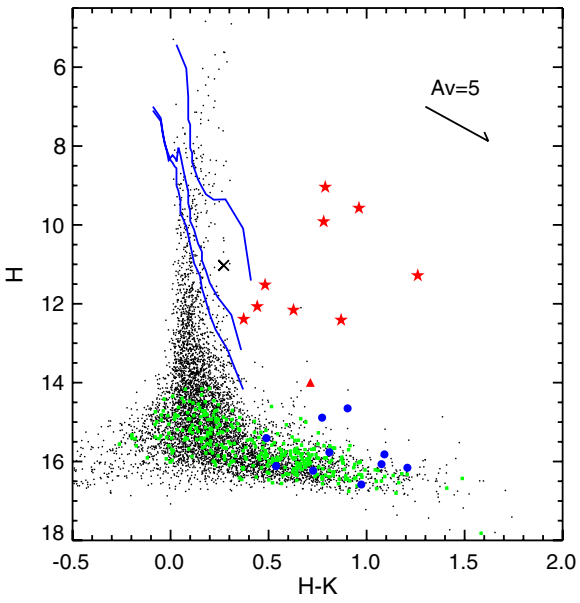

Figure 10. H vs. $H - K_s$ diagram for the sample, with the same notation as earlier figures. The solid blue lines are models from Siess et al. (2000) at 1, 10 and 30 Myr and scaled to 210 pc. The × symbol is the wTTS candidate (2MASS J05060574−0646151; see Section 4.2).

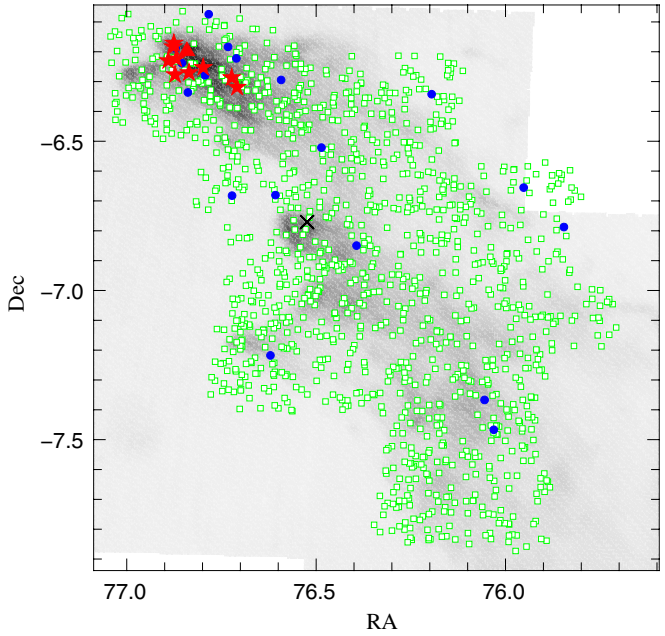

Figure 11. Distribution of our YSO candidates and background galaxies or AGN. Symbols are identical to those in Figure 4. The × symbol is the wTTS candidate (2MASS J05060574−0646151; see Section 4.2). The background gray scale image is the 160 μm MIPS observation of IC 2118.

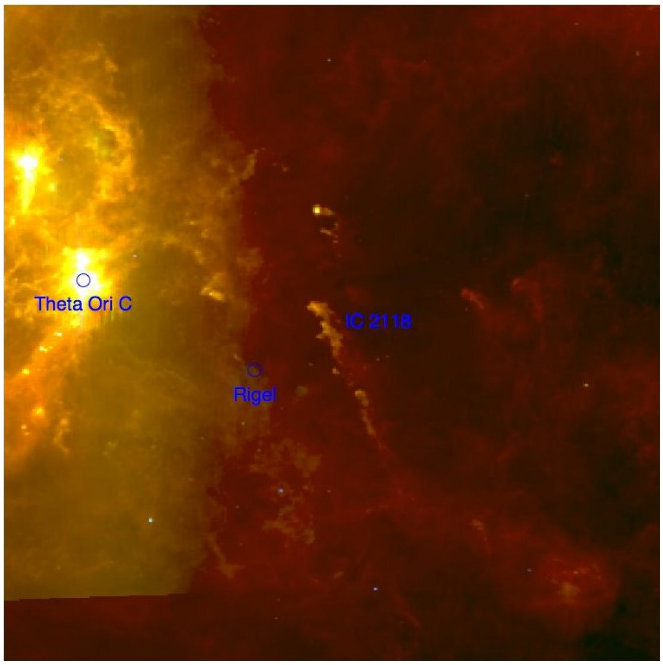

Figure 12. Three-color composite of *IRAS* data at 12, 25, and 100 μm, centered on IC 2118, with a circle at the location of θ^1 Ori C and Rigel. The region shown is ∼19° on a side. This figure illustrates that IC 2118 is one of several nebulae located many degrees from the ONC whose morphology appears "wind-blown" by a source roughly toward the ONC and belt stars.

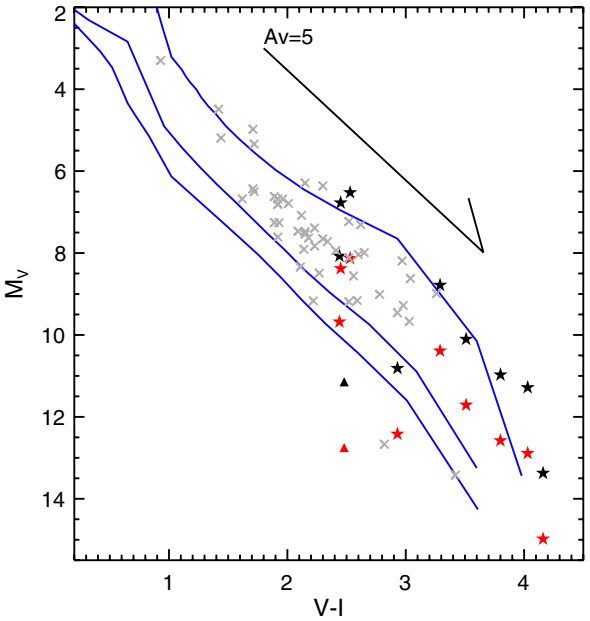

Figure 13. Optical M_V vs. $V - I_c$ color–magnitude diagram. The Siess et al. (2000) isochrones are included (1, 10, and 30 Myr), but shifted to absolute M_V. The black stars/triangle are our YSO candidates, same notation as earlier figures, assuming a distance of 440 pc, and the red stars/triangle are our YSO candidates, assuming a distance of 210 pc. The gray × symbols are Taurus YSOs (from Rebull et al. 2010 and Güdel et al. 2007, and references therein), taken to be at 140 pc; Torres et al. 2007, 2009. The Taurus distribution is broad and there are many fewer IC 2118 stars, but this distribution weakly suggests that IC 2118 is closer rather than farther (see the text).

to an origin roughly between the Trapezium and the Orion belt stars (see Figure 2 of Bally and Figure 2 of OS98). Both Bally and OS98 include IC 2118 as a nebula that exemplifies this pattern. Figure 12, based on *IRAS* data, shows a wide-angle view of the gas and dust west of Orion (centered on IC 2118), illustrating that IC 2118 is simply one of a number of nebulae located many degrees from the ONC whose morphology appears "wind-blown" by a source roughly toward the ONC and belt stars. Detailed examination of the leading edge of the MIPS and IRAC images of IC 2118 (Figures 2 and 3) supports this assertion. The arcs in Figure 3 show that while the morphology seems to better follow the arc from Rigel, the direction of the "windblown" structures in the nebula suggests that the Trapezium is instead the exciting source, or perhaps a structure centered near it, such as the expanding Orion-Eridanus Bubble

(see, e.g., Kun et al. 2001). These arguments therefore support a distance to IC 2118 of order 400 pc.

4.5.2. Arguments in Favor of $d \sim 210$ pc

Rigel ($V \sim 0.3$, spectral type B8I) is located only about 2.°5 from IC 2118, compared to the Trapezium and belt stars at more than 7° distant. In the optical, IC 2118 is normally described as a reflection nebula due to its blue colors and lack of a bright rim. The most obvious photon source—and the one most frequently mentioned in the literature—for illuminating IC 2118 is Rigel. Since, according to Hipparcos, Rigel is at $d \simeq 264 \pm 25$ pc, it follows that IC 2118 should be at a distance of order 250 pc.

As noted by Kun et al. (2001), HD 32925 is located along the line of sight to IC 2118 and appears to have significant reddening ($A_V = 1.36$). This suggests it lies within or behind IC 2118. If one adopts the Walraven photometric distance for HD 32925 (Brown et al. 1994) of $d \sim 260$ pc, this places IC 2118 nearer than this. However, the distance to HD 32925 is not well established. The best spectral type available for HD 32925 is A0III (Houk, Michigan Spectral Catalog); given $V = 9.2$, $M_V = 0.0$ (Schmidt-Kaler 1982) and the A_V, this yields $d \sim 370$ pc. The original Hipparcos catalog parallax for HD 32925 was $\pi = 1.69 \pm 1.35$ mas, hence supporting any distance more than about 250 pc. The new Hipparcos reduction yields $\pi = 3.66 \pm 1.2$ mas, or $d = 273$ (+133, −66) pc. No firm conclusion can be drawn from these disparate estimates.

Figure 13 presents the M_V versus $V - I$ CMD, comparing IC 2118 stars to YSOs in Taurus (with data from Rebull et al. 2010; Güdel et al. 2007, and references therein). Based on morphological grounds (e.g., the degree to which the YSOs are still embedded in their natal gas), we expect that the IC 2118 stars might be slightly younger than the often more physically dispersed Taurus stars. On the other hand, based on the ratio of Class I to Class II sources, the IC 2118 objects might be slightly older than Taurus. In Figure 13, the distribution of IC 2118 objects is broad, but assuming a distance of 440 pc, then IC 2118 appears to be slightly younger than Taurus. Assuming a distance of 220 pc, the bulk of the IC 2118 distribution is comparable to the bulk of the Taurus distribution at ∼3 Myr. Figure 13 thus weakly suggests that IC 2118 is closer rather than farther. A similar calculation with ONC members yields similar results.

4.5.3. No Clear Answer

It is tempting to try to use the infrared colors to set some constraint on the distance, since after all the infrared is reprocessing the UV starlight, and the distance between a given source and the cloud clearly affects the radiation field bathing the cloud. The integrated (over the entire cloud) infrared spectral energy distribution is shown in Figure 14, where for each band, a corresponding background outside the cloud has been subtracted and the images have been smoothed to the lowest angular resolution before the measurements. The figure includes a fit performed using the DUSTEM model using the interstellar standard radiation field (ISRF; Mathis et al. 1983) In a nutshell, the DUSTEM model requires at least three different dust populations (PAHs, very small and big grains) to interpret the infrared dust emissivity (for details see Compiégne et al. 2008, 2010; Désert et al. 1990); plus the incident radiation field that is the sum of the mean ISRF and a stellar component diluted by the distance squared. The fact that the observations are well matched by the standard radiation field immediately indicates that neither θ Ori nor Rigel are dominant sources in illuminating the nebula, and therefore, no simple constraint arises from the mid-IR measurements.

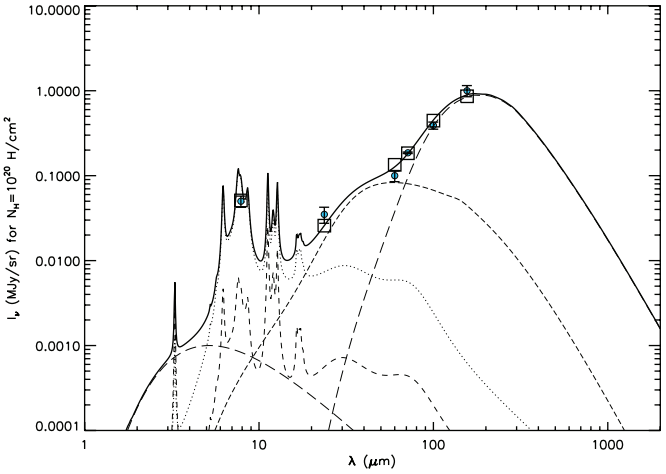

Figure 14. Best model fit to the extended dust emission infrared SED of the IC 2118 cloud itself; see the text. The observed SED is plotted with circles and error bars, the modeled SED with boxes. Both are normalized to 160 μm. The solid line is the total dust emission spectrum; the other five lines are the different dust components (PAHs, dotted and medium dashed lines with emission features, from the cations and neutrals; stochastically heated very small grains, long-dashed line, warmest blackbody curve; Big Grains at thermal equilibrium, long-dashed cool blackbody curve; the smooth curve that peaks around 2–3 μm, short dashed line, is a component added in to explain the near-IR continuum, see Flagey et al. 2006, and references therein). The observations are well-matched by the standard radiation field, suggesting that neither θ Ori nor Rigel are dominant sources in illuminating IC 2118.

Unfortunately, it is our opinion that the evidence currently available pertaining to the distance to IC 2118 is not definitive. The upcoming *GAIA* mission could provide a definitive answer by deriving accurate parallaxes for HD 32925 and/or for the brighter YSOs of IC 2118. A spectral type for the diffuse optical emission from IC 2118 could establish whether the dominant photon source is Rigel or the hotter, earlier type stars of the ONC or belt region.

4.6. J05080318−0617141: A High Proper Motion Star

While constructing three-color images using *Spitzer* and POSS images, we noticed one object projected onto the nebulosity that appeared to have moved significantly between the epoch of the POSS image and the current epoch; see Table 5. This object, J05080318−0617141, moves at a steady rate of ∼0.2 arcsec yr^{-1} between the 1955 and 2000 epochs; at a distance of 210 pc, this would be ∼180 km s^{-1}. The object does not appear to move much between the 2MASS and IRAC epochs (2000–2005); five years may not have been enough time to see significant motion. Our optical observations (from 2007) do not have precise enough astrometry for this calculation. However, this object is in the USNO-B catalog of objects with measurable proper motion; it is object 0837–0052579, having $\mu_\alpha = 134$ mas yr^{-1} and $\mu_\delta = -86.0$ mas yr^{-1}, quite comparable with the net ∼0.2 arcsec yr^{-1} noted above.

We were granted two nights at the Palomar 200″ in 2007 Jan to obtain follow-up spectroscopy of our YSO candidates. Unfortunately, due to high velocity winds, high clouds, and poor seeing on both of our nights, little of our data were usable. However, the spectrum we obtained of this relatively bright, high proper motion object reveals it to be an M star.

We do not find an IRAC excess for this object, and it is not detected at 24 μm. We have optical and near-infrared measurements: $U = 18.77$, $V = 15.98$, $R_c = 14.62$, $I_c = 13.19$, $J = 11.68$, $H = 11.08$, and $K_s = 10.85$ (where the near-infrared

Table 5
Observations of J05080318−0617141

Data Set	Position (J2000)	Date of Observation (UT)	Notes
POSS-1	05:08:02.77 −06:17:10.0	1955 Dec 15 07:50	
POSS-2	05:08:03.00 −06:17:11.9	1985 Jan 20 11:26	
2MASS	05:08:03.19 −06:17:14.1	2000 Oct 12 09:04	JHK_s images have a nearby "persistence artifact"
IRAC	05:08:03.18 −06:17:14.1	2005 Mar 25 00:02	Large PSF
Our optical	05:08:03.2 −06:17:14	2007 Jan 09 02:50	Large errors on astrometry

points come from 2MASS, and the error on all the optical points is ∼0.03 mag). Using the $V/V-I_c$ diagram and the models from Siess et al. (2000), it is likely to be an M2 to M5 star between 20 and 70 pc away. Assuming those distances, its projected space motion is between ∼20 and 60 km s^{-1}.

5. DISCUSSION AND CONCLUSIONS

By using *Spitzer* to search for objects with infrared excess in the IC 2118 region, we have doubled the inventory of YSOs and YSO candidates, in the region for which we have both IRAC and MIPS data, from 5 (4 CTTS and 1 WTTS) to 11 (6 new candidates selected via *Spitzer* colors, plus the 4 CTTS and 1 WTTS from before). Including the YSOs found by Kun and collaborators outside our surveyed region, the total number of YSOs found in this region is between 15 and 17, depending on the membership status of 2 objects from Kun et al. (2004) whose membership is questionable. Most of the confirmed YSOs, and all of the new objects, are found in the "head" of the nebula, the cloud G 206.4-26.0 from Kun et al. (2001). This cloud is estimated to be 85 $M_\odot$ total molecular mass (Kun et al. 2001). If we assume that all 10 YSOs located in the head of the Nebula are legitimate members of the cluster and on average 0.5 $M_\odot$, then ∼5% of the cloud's mass is in stars, which is a slightly higher star formation efficiency than could have been calculated before.

The SEDs of all 10 of these objects are similar (Class II); 050729.4−061637 is the exception, with a flat SED that is much different than the others. The edge-on disk candidate 050721.9−061152 has only a reasonably small excess until 24 μm. All 10 of these objects are within ∼13′; assuming a distance of 210–400 pc, these objects are all within ∼0.8–1.6 pc of each other.

In Perseus and other regions (Rebull et al. 2007, and references therein), several small groups of likely young stars are found within a parsec of each other. Notably, they have a large range of SED types, in one case (Per 6) ranging from apparent photospheres to Class 0 candidates and an apparently starless millimeter continuum core. The fact that the range of SED types is much smaller in the case of IC 2118 may simply be a result of the much lower extinction toward IC 2118, or that the stars in IC 2118 are old enough that any differences in the timescales of very early star formation (e.g., as a result of different initial disk masses or rotation rates) are wiped out, or it could be telling us something about the onset of star formation in these two different regions. There is no clear evidence that the stars in Perseus are a result of triggered star formation, but the literature suggests that IC 2118 was triggered. A wide range of SED types can also be found in the cometary cloud L1251 (see, e.g., Lee et al. 2006), suggesting that perhaps triggering may not result in a small range of SED types.

If this region is indeed triggered star formation, then we might be able to find trends of age or mass with location. For example, Kun et al. (2004) asserts that stars closer to center of the core should be younger. Since there are so few objects, since the distance is uncertain, and since we do not have spectral types for most of these objects, we can not do this rigorously; we can look at size of infrared excess, which is often taken as a proxy for age, e.g., in the Class 0/I/flat/II/III scheme. There is no clear correlation of various measures of IR excess and location in the cloud. This must be, at least in part, because so many of the SEDs are similar.

Additional follow-up spectroscopic data are needed in the IC 2118 region to confirm or refute the YSO status of the six new objects with infrared excesses, some of which appear to also have ultraviolet excesses, and all of which have optical magnitudes compatible with being YSOs in IC 2118. The new edge-on disk candidate in particular warrants further study, since such objects are relatively rare.

The distance to IC 2118 is still uncertain, with evidence to be found for both ∼210 and ∼440 pc. *GAIA* will be needed to resolve this mystery.

We acknowledge all of the students who contributed their time and energy to early reductions, analysis, discussion, and poster papers based on this work. They include the following, from 2005–2007. From Oil City Area Senior High School (w/T. Spuck): D. H. Bowser II, B. R. Ehrhart, I. Frost, M. T. Heath, N. Kelley, P. Morton, M. Walentosky, S. P. Weiser, and D. Yeager. From Phillips Exeter Academy (w/A. Maranto): M. T. Greer, J. V. Preis, and P. D. Weston. From Lincoln High School (w/B. Sepulveda): A. S. Hughes, S. Meyer, N. D. Sharma, and E. Sharma. From Luther Burbank High School (w/C. Weehler): J. M. Herrera.

We also acknowledge conversations with Gaspard Duchene regarding our edge-on disk candidate and fluxes for some comparison SEDs.

This work is based in part on observations made with the *Spitzer Space Telescope*, which is operated by the Jet Propulsion Laboratory, California Institute of Technology, under a contract with NASA. Support for this work was provided by NASA through an award issued by JPL/Caltech. This work was also supported by the Spitzer Research Program for Teachers and Students.

The research described in this paper was partially carried out at the Jet Propulsion Laboratory, California Institute of Technology, under contract with the National Aeronautics and Space Administration.

We thank the Palomar Observatory and of course the Spitzer staff for their assistance using the telescope.

This research has made use of NASA's Astrophysics Data System (ADS) Abstract Service, and of the SIMBAD database, operated at CDS, Strasbourg, France. This research has made use of data products from the Two Micron All-Sky Survey (2MASS), which is a joint project of the University of Massachusetts and the Infrared Processing and Analysis Center, funded by the National Aeronautics and Space Administration

and the National Science Foundation. These data are served by the NASA/IPAC Infrared Science Archive, which is operated by the Jet Propulsion Laboratory, California Institute of Technology, under contract with the National Aeronautics and Space Administration. This research has made use of the Digitized Sky Surveys, which were produced at the Space Telescope Science Institute under U.S. Government grant NAG W-2166. The images of these surveys are based on photographic data obtained using the Oschin Schmidt Telescope on Palomar Mountain and the UK Schmidt Telescope. The plates were processed into the present compressed digital form with the permission of these institutions.

REFERENCES

Arthur, N. Cox 2001, Allen's Astrophysical Quantities (4th ed.; New York: Springer)
Ballesteros-Paredes, J., Klessen, R. S., Mac Low, M.-M., & Vazquez-Semadeni, E. 2007, in Protostars and Planets V, ed. B. Reipurth, D. Jewitt, & K. Keil (Tucson, AZ: Univ. Arizona Press), 63
Bally, J., Langer, W. D., Wilson, R. W., Stark, A. A., & Pound, M. W. 1991, in IAU Symp. 147, Fragmentation of Molecular Clouds and Star Formation, ed. E. Falgarone, F. Boulanger, & G. Duvert (Dordrecht: Kluwer), 11
Bessell, M. S. 1979, PASP, 91, 589
Briceño, C., et al. 2007, in Protostars and Planets V, ed. B. Reipurth, D. Jewitt, & K. Keil (Tucson, AZ: Univ. Arizona Press), 345
Brown, A. G. A., de Geus, E. J., & de Zeeuw, P. T. 1994, A&A, 289, 101
Burrows, C. J., et al. 1996, ApJ, 473, 437
Cohen, M. 1980, AJ, 85, 29
Compiégne, M., et al. 2008, A&A, 491, 797
Compiégne, M., et al. 2010, A&A, submitted
Désert, F.-X., et al. 1990, A&A, 237, 215
Duchene, G., et al. 2010, ApJ, 712, 112
Fazio, G. G., et al. 2004, ApJS, 154, 10
Flagey, N., Boulanger, F., Verstraete, L., Miville Deschenes, M. A., Noriega Crespo, A., & Reach, W. T. 2006, A&A, 453, 969
Gautier, T. N., III, et al. 2007, ApJ, 667, 527
Gordon, K. D., et al. 2007, PASP, 119, 1019
Güdel, M., et al. 2007, A&A, 468, 353
Guieu, S., et al. 2009, ApJ, 697, 787
Gutermuth, R. A., et al. 2008, ApJ, 674, 336
Gutermuth, R. A., et al. 2009, ApJS, 184, 18
Jeffries, R. D., Oliveira, J. M., Naylor, T., Mayne, N. J., & Littlefair, S. P. 2007, MNRAS, 376, 580
Kun, M., & Nikolic, S. 2003, Commmunications of the Konkoly Observatory Hungary 103, ed. Cs. Kiss, M. Kun, & V. Könyves (Budapest: Eötvös Loránd Univ.), 19
Kun, M., Prusti, T., Nikolić, S., Johansson, L. E. B., & Walton, N. A. 2004, A&A, 418, 89
Kun, M., et al. 2001, PASJ, 53, 1063
Lada, C. J. 1987, in IAU Symp. 115, Star Forming Regions, ed. M. Peimbert & J. Jugaku (Dordrecht: Reidel Pub.), 1
Lee, H.-T., & Chen, W. P. 2007, ApJ, 657, 884
Lee, H.-T., Chen, W. P., Zhang, Z.-W., & Hu, J.-Y. 2005, ApJ, 624, 808
Lee, J.-E., et al. 2006, ApJ, 648, 491
Lejeune, T., Cuisinier, F., & Buser, R. 1997, A&AS, 125, 229
Lejeune, T., Cuisinier, F., & Buser, R. 1998, A&AS, 130, 65
Lonsdale, C. J., et al. 2003, PASP, 115, 897
Makovoz, D., & Marleau, F. R. 2005, PASP, 117, 1113
Mathis, J. S., et al. 1983, A&A, 128, 212
Menten, K. M., Reid, M. J., Forbrich, J., & Brunthaler, A. 2007, A&A, 474, 515
Ogura, K., & Sugitani, K. 1998, PASA, 15, 91
Rebull, L. M., et al. 2000, AJ, 119, 3026
Rebull, L. M., et al. 2007, ApJS, 171, 447
Rebull, L. M., et al. 2010, ApJS, 186, 259
Rieke, G. H., et al. 2004, ApJS, 154, 25
Schmidt-Kaler, T. 1982, Bull. Inf. Cent. Donnees Stellaires, 23, 2
Siess, L., Dufour, E., & Forestini, M. 2000, A&A, 358, 593
Skrutskie, M. F., et al. 2006, AJ, 131, 1163
Stansberry, J. A., et al. 2007, PASP, 119, 1038
Stauffer, J. R., et al. 2007, ApJS, 172, 663
Surace, J. A., et al. 2004, VizieR Online Data Catalog, 2255, 0
Torres, R. M., Loinard, L., Mioduszewski, A. J., & Rodríguez, L. F. 2007, ApJ, 671, 1813
Torres, R. M., Loinard, L., Mioduszewski, A. J., & Rodríguez, L. F. 2009, ApJ, 698, 242
van Leeuwen, F. 2007, A&A, 474, 653
Werner, M. W., et al. 2004, ApJS, 154, 1
Wilking, B. A., Bontemps, S., Schuler, R. E., Greene, T. P., & André, P. 2001, ApJ, 551, 357